

Supplementary Material

Bigg immersion-freezing and Meyers contact-freezing

The influence of immersion- and contact-freezing within the Morrison et al. (2005) microphysics scheme was tested to quantify their contribution to N_{ice} . Simulations with contact-freezing (Meyers et al. 1992 - hereafter, M92) and immersion-freezing (Bigg 1953 - hereafter, B53) switched either on or off are shown in Fig. S1. The addition of B53 and M92 produces a significantly larger ice crystal number concentration (up to 3 L^{-1} , 1.5 L^{-1} , and 10 L^{-1} in cases 1, 2, and 3 respectively) than the mean observed ($0.47 \pm 0.86 \text{ L}^{-1}$, $0.35 \pm 0.20 \text{ L}^{-1}$, and $0.55 \pm 0.95 \text{ L}^{-1}$ respectively, Table 2).

Modelled ice number concentrations with and without B53 and M92 active are similar in case 1. Both representations cause glaciation, and liquid water is not modelled at any point during the simulations. No improvement can be seen in the liquid water mixing ratio when both the B53 and M92 nucleation mechanisms are disabled. Modelled ice number concentrations for case 2 peak at $\sim 1.5 \text{ L}^{-1}$ and $\sim 0.8 \text{ L}^{-1}$ with and without both B53 immersion- and M92 contact-freezing nucleation active. Both scenarios allow for liquid water to form in the cloud, with $\sim 0.2 \text{ g kg}^{-1}$ modelled. When B53 and M92 are active in case 3, high ice number concentrations are rapidly simulated at approximately 12 h-14 h. This event causes the evaporation of all simulated liquid water, and the region of high ice number concentration dissipates back to the original sustained concentration of $\sim 2 \text{ L}^{-1}$ afterwards. This event is not simulated when B53 and M92 are disabled, suggesting these additional sources of ice number are the cause of this phenomenon.

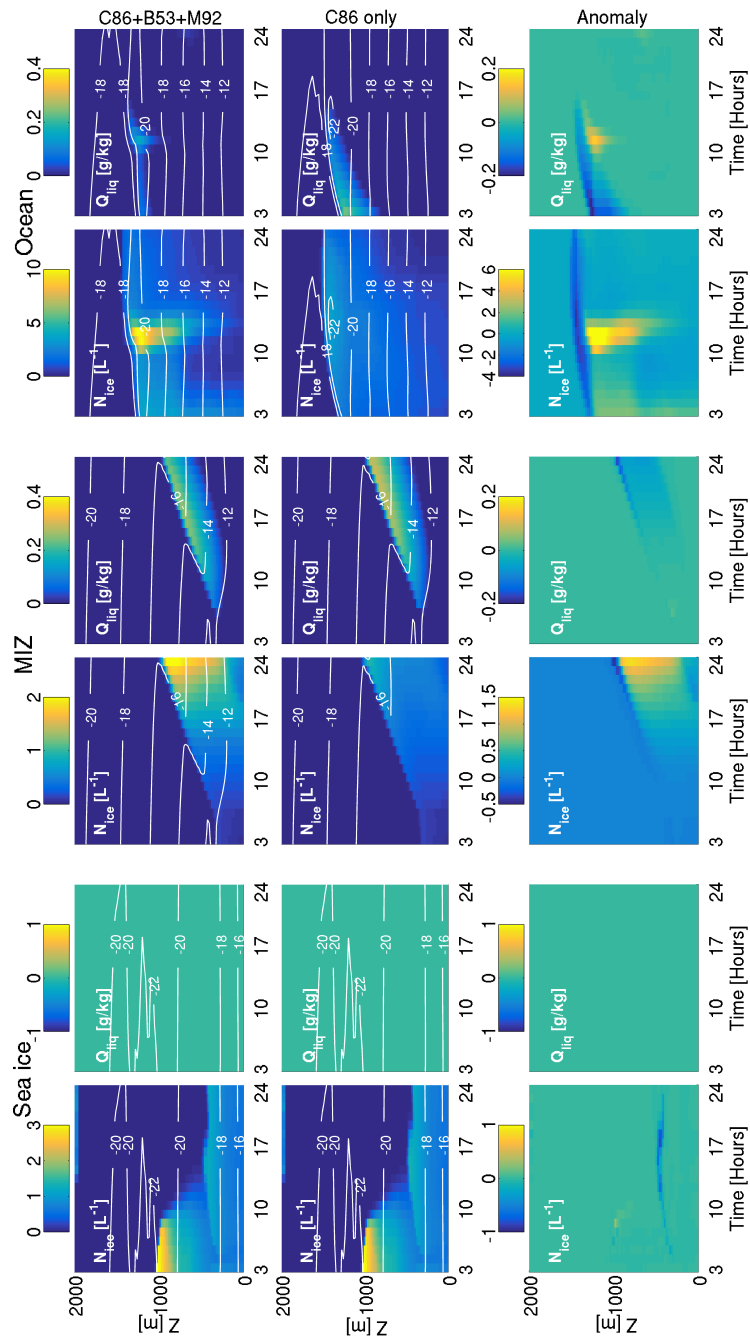


Figure S1. Simulated ice number concentrations (N_{ice} , **columns 1, 3, and 5**) and liquid water mixing ratios (Q_{liq} , **columns 2, 4, and 6**) using the Cooper (1986) parameterisation under default WRF conditions ($T < -8^{\circ}C$, $S_w > 0.999$ or $S_i > 1.08$). **Top row:** B53, M92, and C86 active. **Middle row:** C86 deposition-condensation freezing only. **Bottom row:** Anomaly between simulations including B53 and M92 and those using C86 only. **Column 1-2:** Sea ice (case 1), **Column 3-4:** MIZ (case 2), **Column 5-6:** Ocean (case 3). Run length 24 hours. Temperature ($^{\circ}C$) contours are overlaid in white.

Supplementary figures

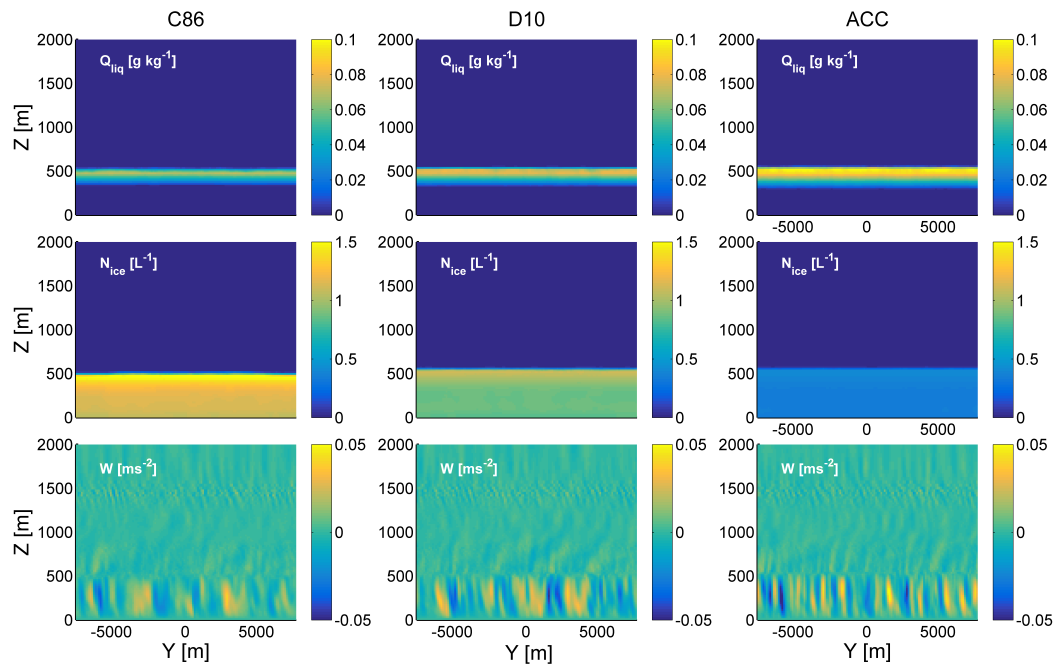


Figure S2. Z-Y slice of modelled Q_{liq} (**top row**), N_{ice} (**middle row**), and vertical velocity (**bottom row**) at 21 h over the sea ice (case 1). The N_{ice} and Q_{liq} fields are homogeneous, with liquid layer at cloud top and ice formation throughout. Enhanced turbulent activity, due to the comparatively larger liquid water content, is modelled with ACC.

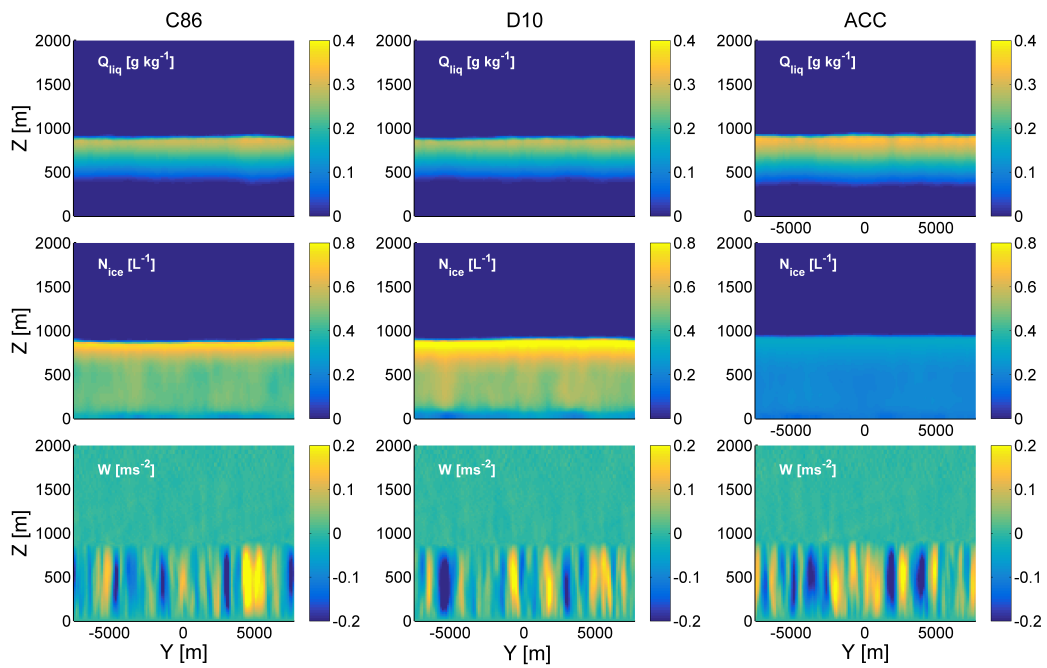


Figure S3. Z-Y slice of modelled Q_{liq} (**top row**), N_{ice} (**middle row**), and vertical velocity (**bottom row**) at 21 h over the MIZ (case 2). Significant turbulence is simulated within the cloudy layer (bottom row). With comparison to the sea ice case, the liquid layer at cloud top is more heterogeneous in all cases. This is particularly clear in the D10 simulations, where N_{ice} is enhanced in downdraughts.

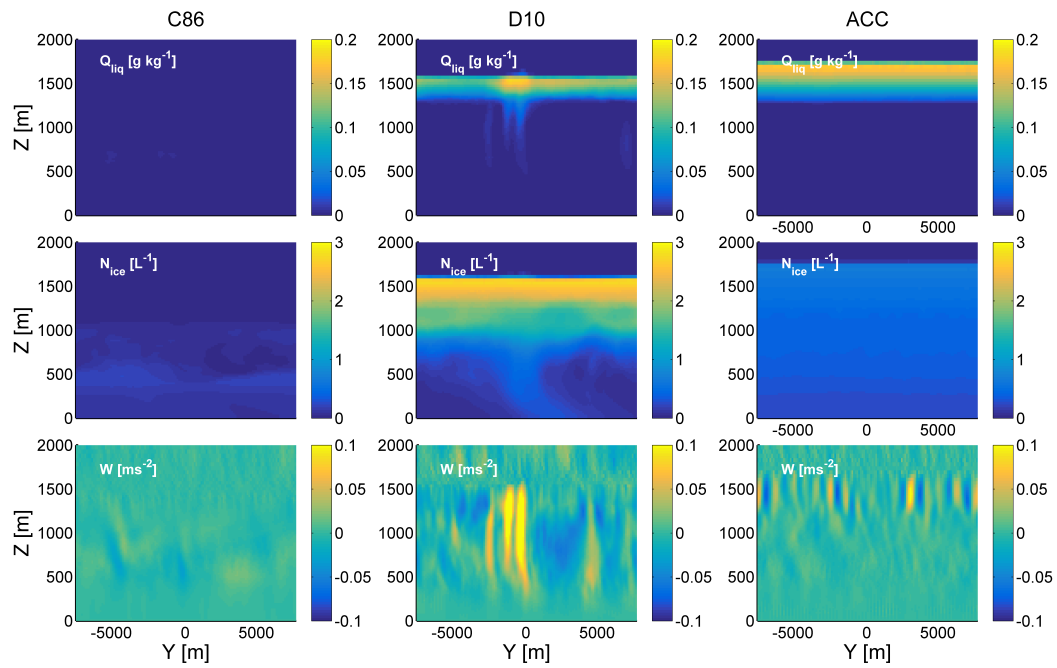


Figure S4. Z-Y slice of modelled Q_{liq} (**top row**), N_{ice} (**middle row**), and vertical velocity (**bottom row**) at 21 h over the ocean (case 3). Large updraught columns are simulated using D10, which correspond spatially with columns of high Q_{liq} . These updraughts are co-located with a precipitating (snow) region, evident from the N_{ice} figures (second row). C86 had dissipated by 21 h; therefore, little activity can be seen in this simulation. Similar to cases 1 and 2, ACC produces a homogeneous liquid layer at cloud top, with ice below.

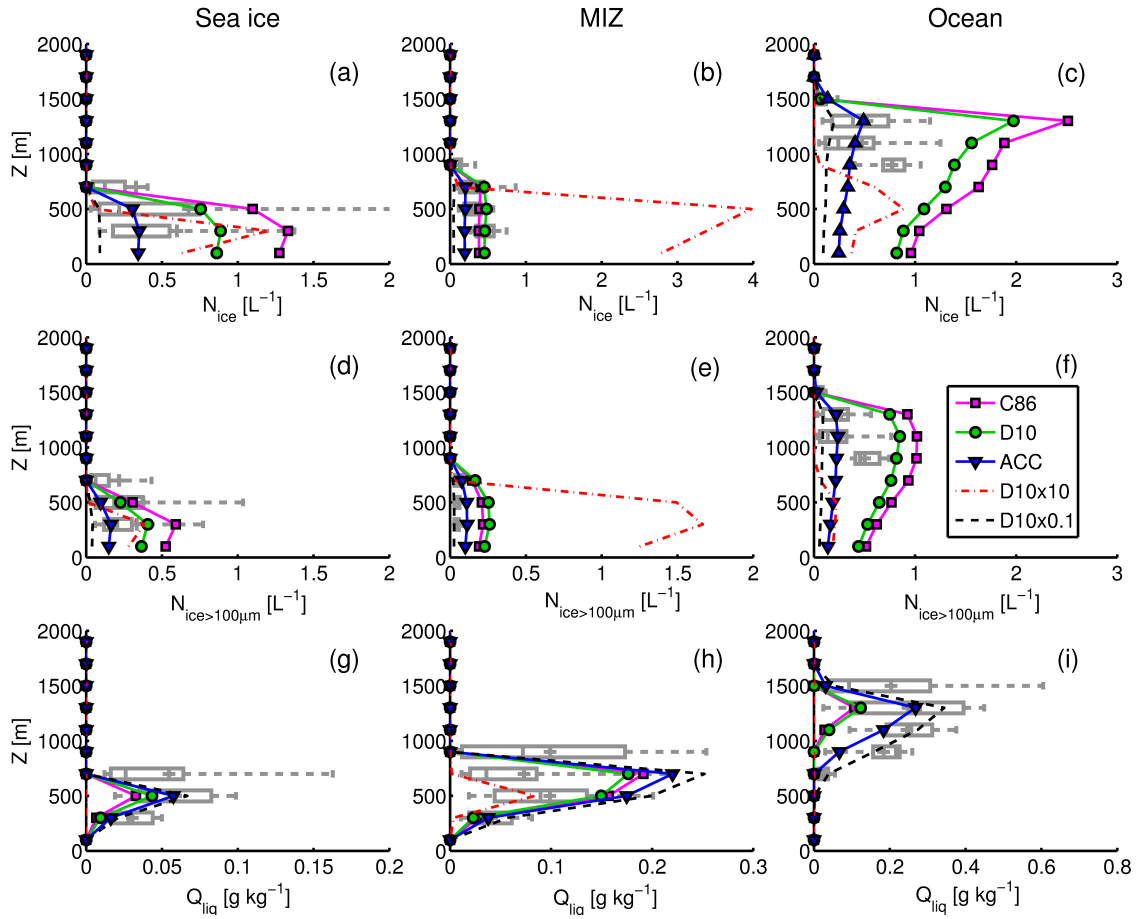


Figure S5. Observed N_{ice} (top row), $N_{ice>100\mu m}$ (middle row), and Q_{liq} (bottom row) for the sea ice (column 1), MIZ (column 2) and ocean (column 3) cases. Observations are shown as grey boxes. These boxes illustrate data similarly to those in Fig. 7. Modelled N_{ice} , $N_{ice>100\mu m}$, and Q_{liq} are overlaid from the C86 (magenta), D10 (green), ACC (blue), D10 \times 10 (red), and D10 \times 0.1 (black) simulations. Model time steps of 21 h, 17 h, and 7 h are again used for comparison with the sea ice, MIZ, and ocean observations respectively.

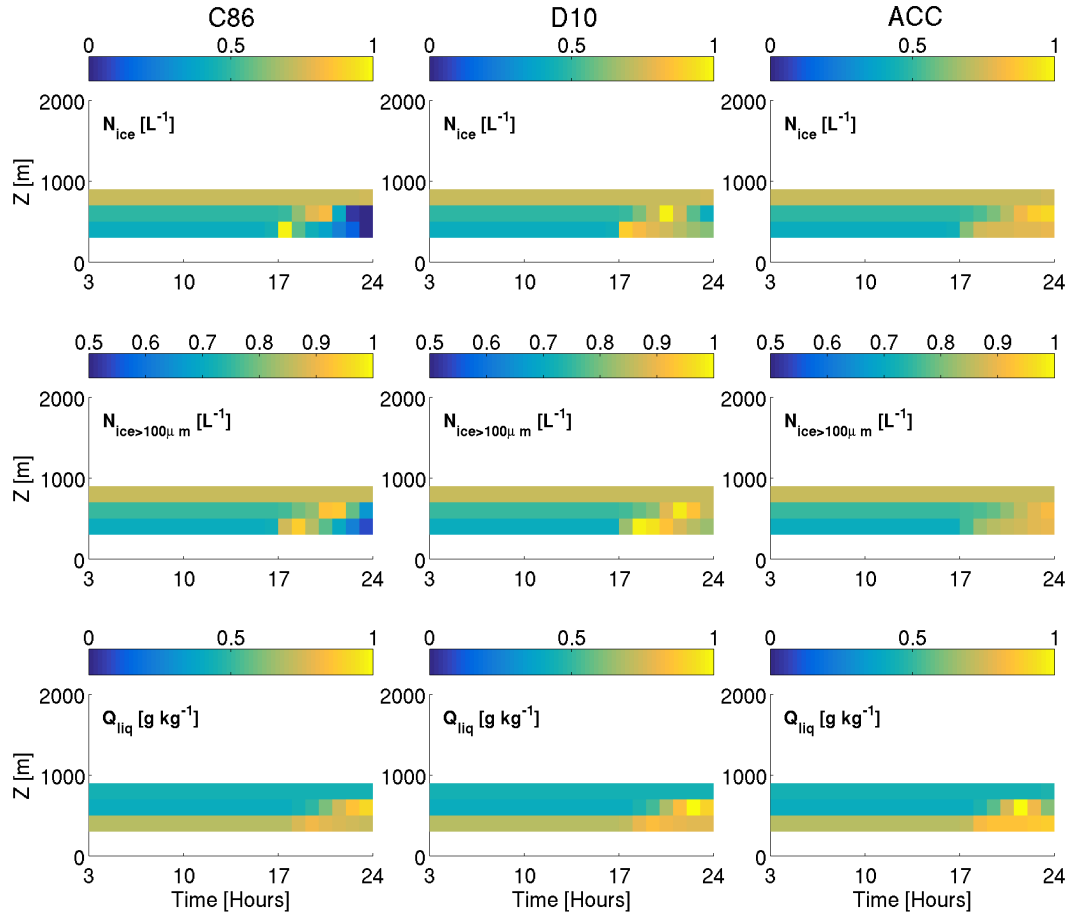


Figure S6. Residual comparison of modelled and observed N_{ice} (**top row**), $N_{ice > 100 \mu m}$ (**middle row**), and Q_{liq} (**bottom row**) in case 1 (sea ice) for each model time step. At each altitude bin, the mean observed quantity is subtracted from the mean modelled. The absolute magnitude of this fraction is then subtracted from 1. Therefore, better agreement between the mean observed and mean modelled values gives a larger fraction (with a maximum of 1). When two of the three parameterisations give good agreement with the N_{ice} observations at the same time step, that time step has been selected for comparison with the observations in Fig. 7. For the sea ice simulations, the chosen time step was 21 h.

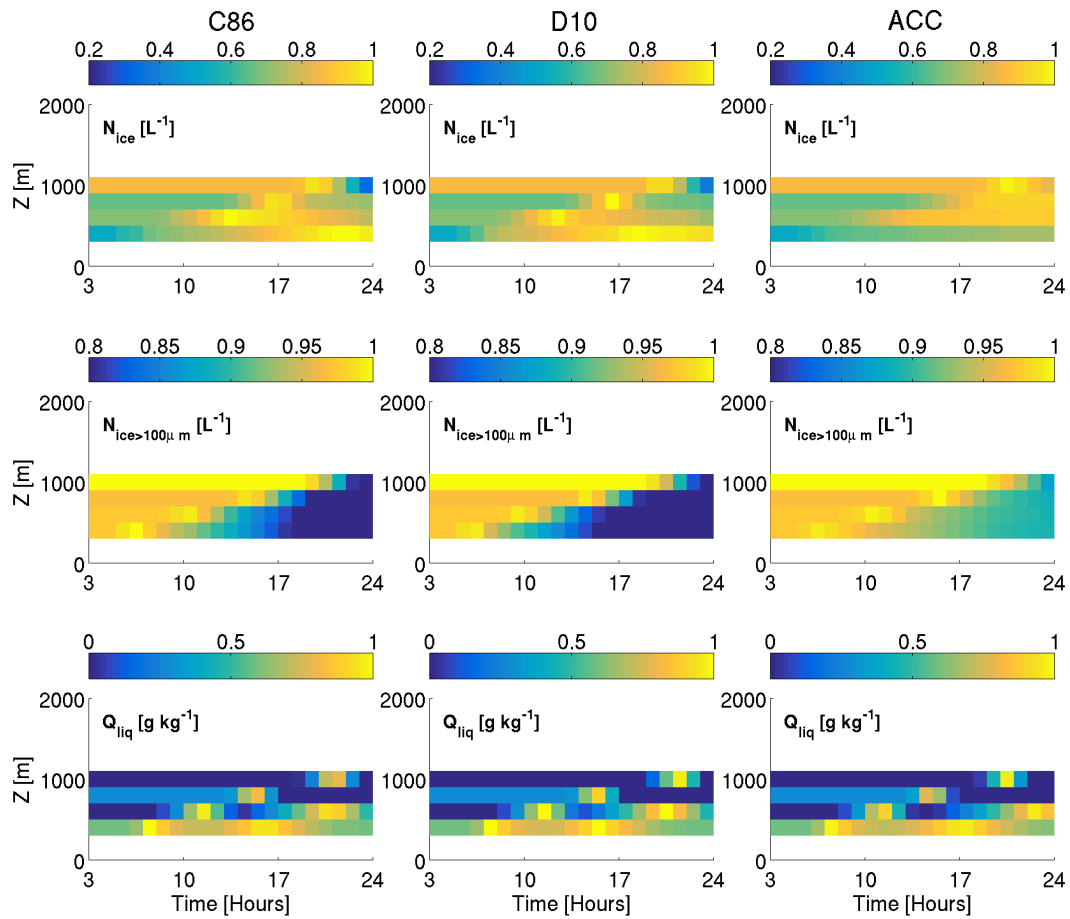


Figure S7. Residual comparison of modelled and observed N_{ice} (**top row**), $N_{ice>100\mu m}$ (**middle row**), and Q_{liq} (**bottom row**) in case 2 (MIZ) for each model time step. As with Fig. S6, better agreement with the mean observed value gives a larger fraction (with a maximum of 1). For the MIZ simulations, the chosen time step was 17 h.

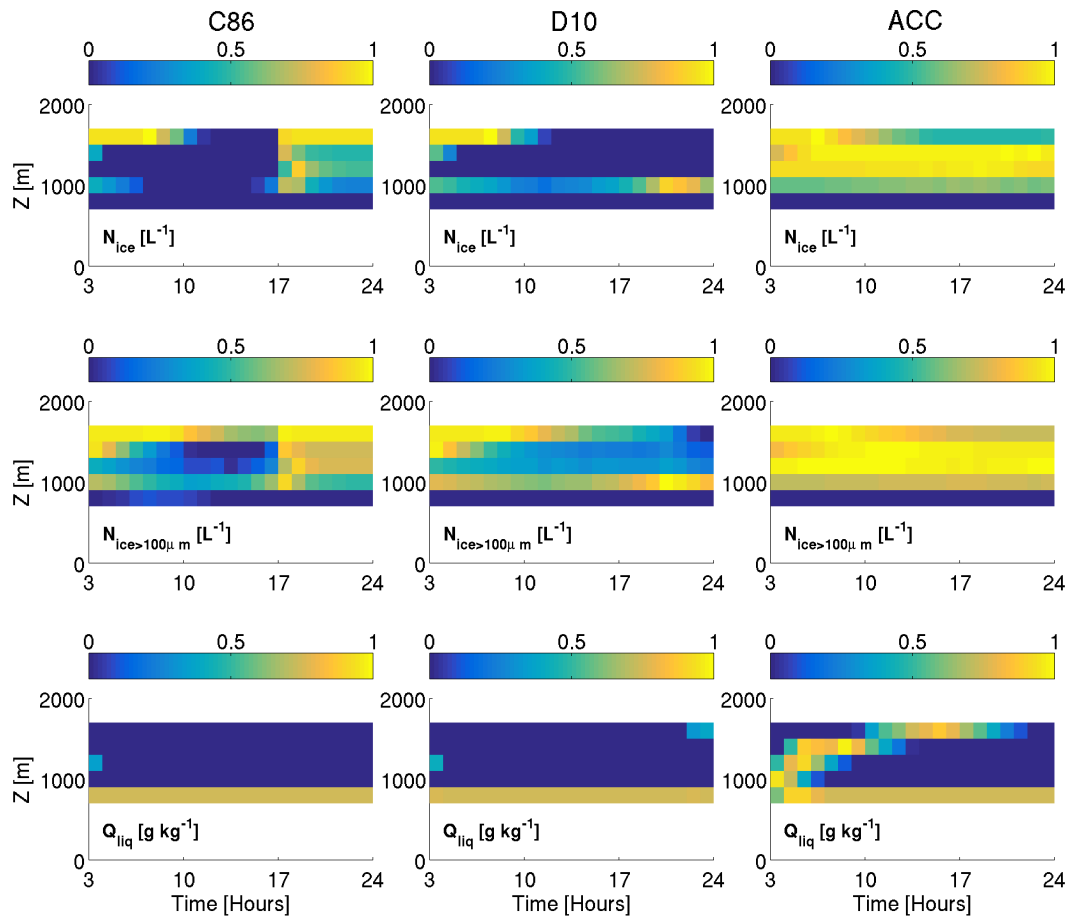


Figure S8. Residual comparison of modelled and observed N_{ice} (**top row**), $N_{ice>100\mu m}$ (**middle row**), and Q_{liq} (**bottom row**) in case 3 (ocean) for each model time step. As with Fig. S6, better agreement with the mean observed value gives a larger fraction (with a maximum of 1). For the MIZ simulations, the chosen time step was 7 h.

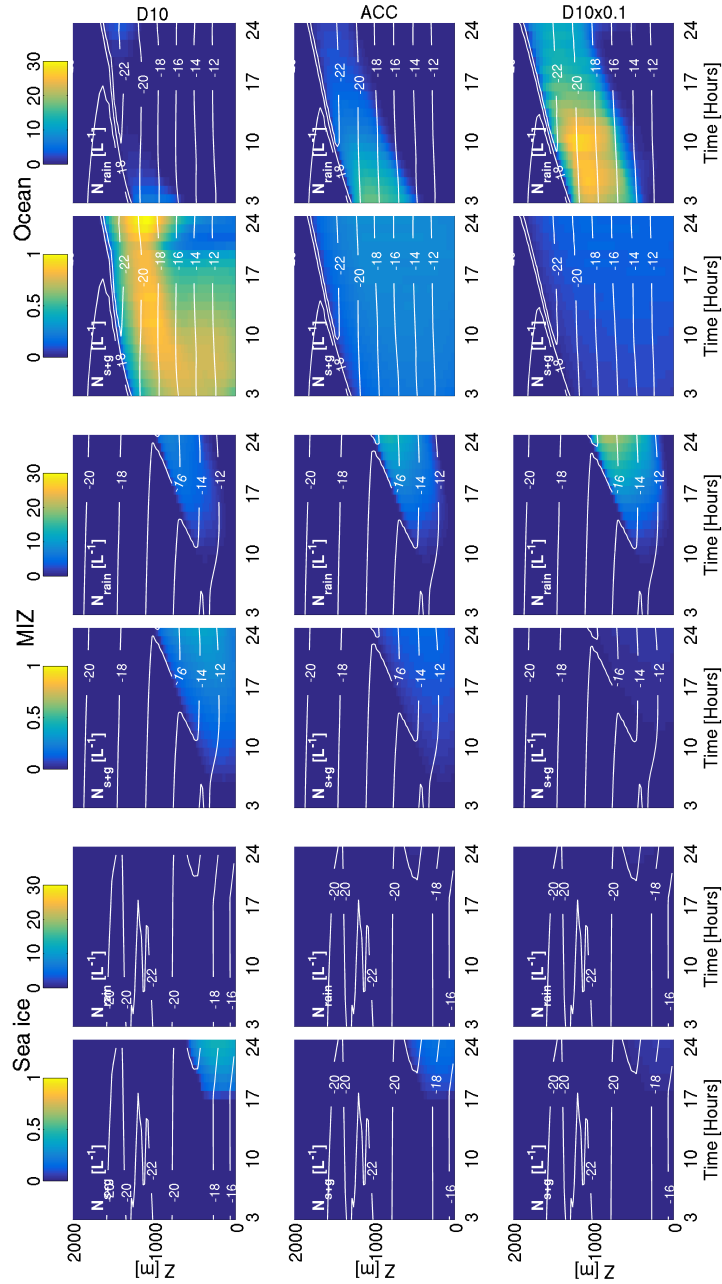


Figure S9. Summed snow and graupel number concentrations (N_{s+g} , **columns 1, 3, and 5**) and rain number concentration (N_{liq} , **columns 2, 4, and 6**) using D10 (**top row**), ACC (**middle row**) and D10 \times 0.1 (**bottom row**). **Column 1-2:** Sea ice (case 1), **Column 3-4:** MIZ (case 2), **Column 5-6:** Ocean (case 3). Run length 24 hours. Solid precipitation increases with simulation time in all cases when using D10, and the rain number concentration behaves similarly in case 2 when applying D10 \times 0.1. Overall, little solid and liquid precipitation is modelled during the ACC simulations, and almost no precipitation is modelled in case 1 with D10 \times 0.1.

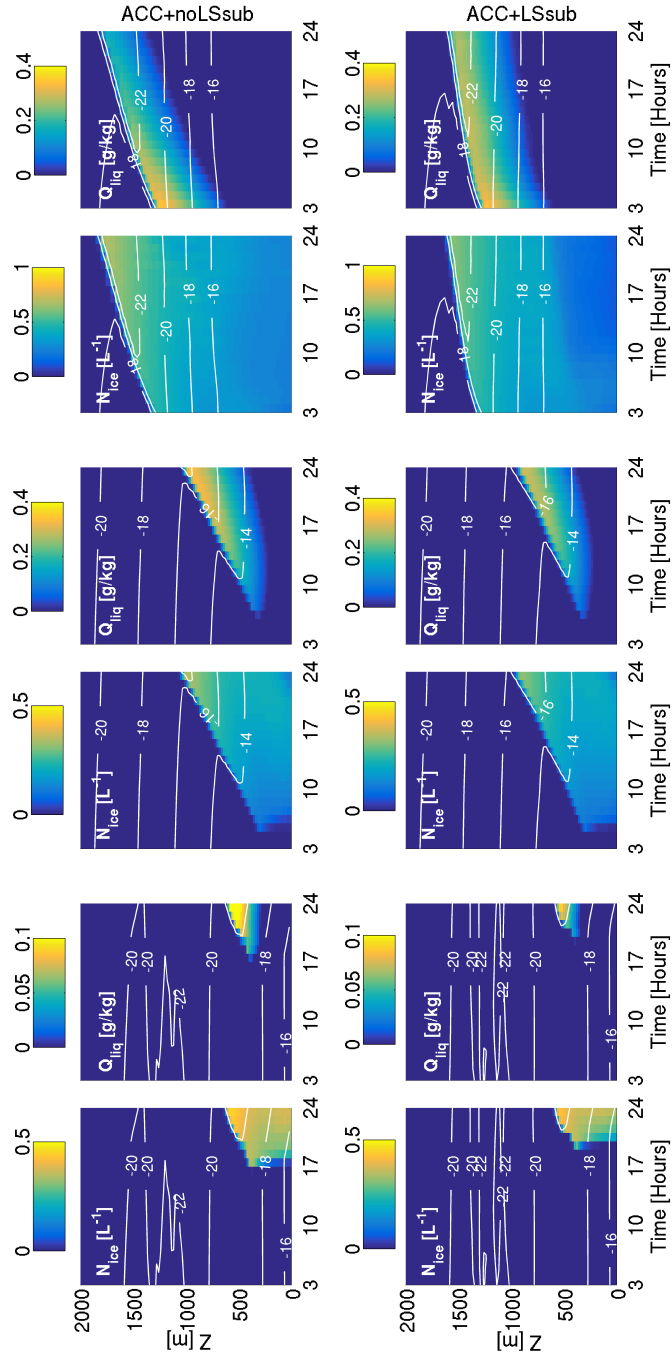


Figure S10. Simulated ice number concentrations (N_{ice} , **columns 1, 3, and 5**) and liquid water mixing ratios (Q_{liq} , **columns 2, 4, and 6**) using ACC without large-scale subsidence (**top row**) and with an imposed subsidence of $2.5 \times 10^{-6} \text{ s}^{-1}$ (**bottom row**, as in Solomon et al., 2015). All are restricted to water-saturation. **Column 1-2:** Sea ice (case 1), **Column 3-4:** MIZ (case 2), **Column 5-6:** Ocean (case 3). Run length 24 hours. In all cases, cloud top height and Q_{liq} is suppressed when large-scale subsidence is imposed. Temperatures are also warmer; however, case 2 is still too cold with comparison to the observations.

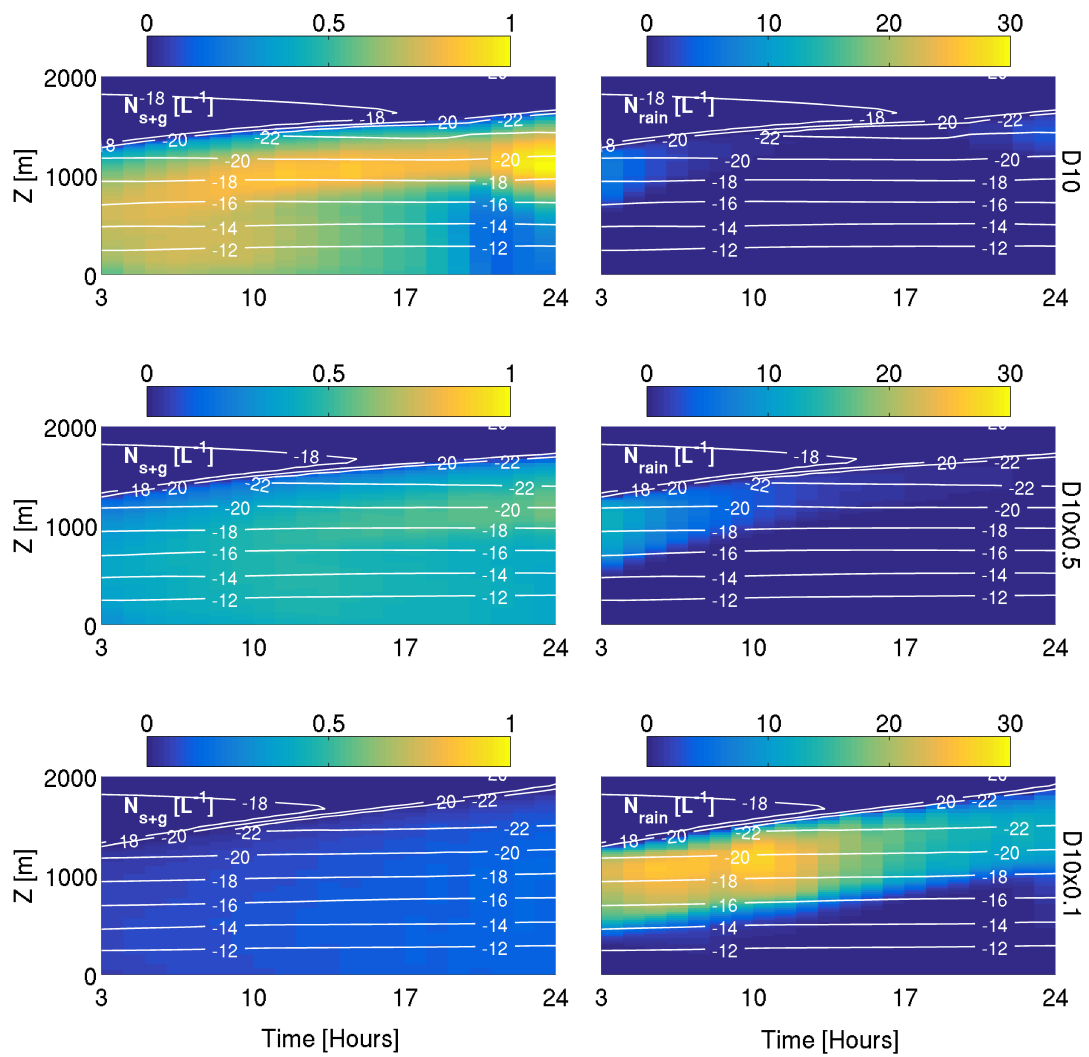


Figure S11. Number concentrations of solid (snow + graupel, N_{s+g} , **left column**) and liquid (rain, N_{rain} , **right column**) precipitation modelled during the D10, D10x0.5, and D10x0.1 simulations over the ocean (case 3).

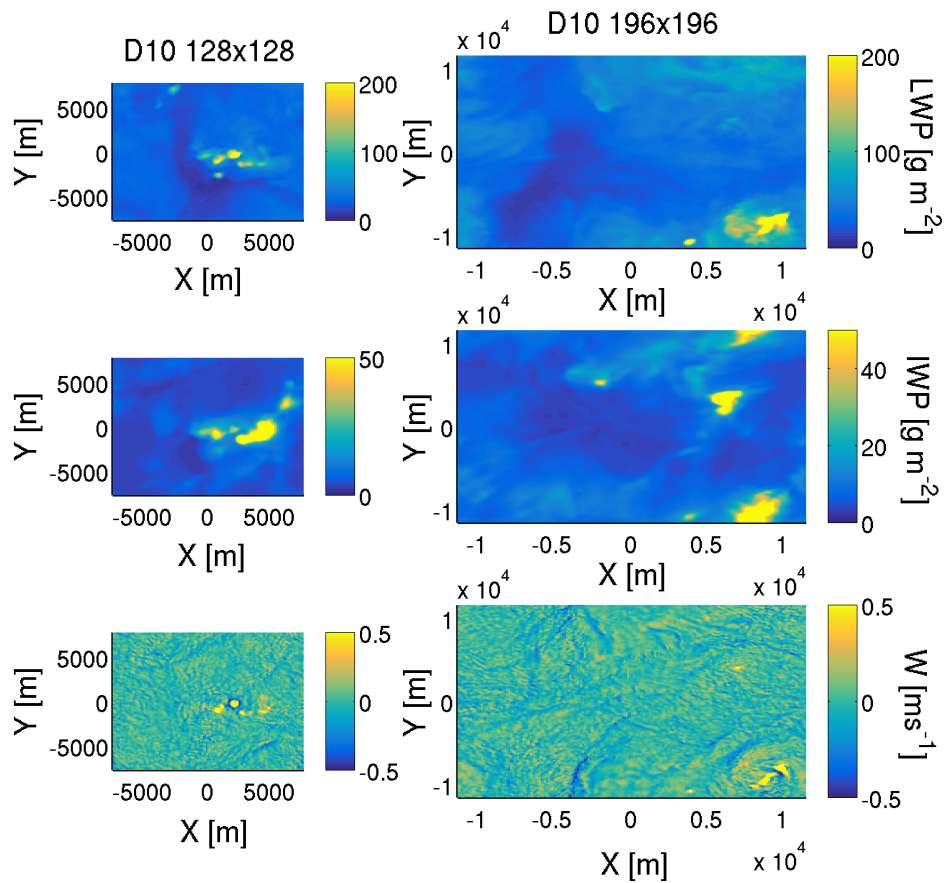


Figure S12. Modelled LWP (**top row**), IWP (**second row**), and W (at approximately 1500 m, **bottom row**) for domain sizes 128×128 grid points (**left column**) and 196×196 grid points (**right column**) at 21 h into the simulations. Both domains use X/Y resolution of 120 m and use the same vertical domain size and resolution; the only difference is the domain size in X/Y. Convective cells – as shown by the hot-spots in LWP, IWP, and W – form in both cases, suggesting that these phenomena were not a result of the original domain specifications.

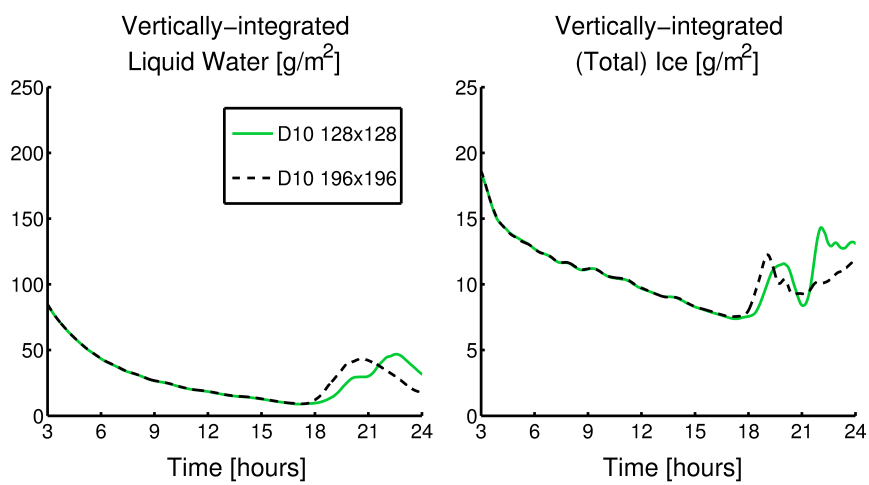


Figure S13. Modelled LWP (**left panel**) and IWP (**right panel**) with time for the original domain size (128×128 grid points, **green**) and the larger domain size (196×196 grid points, **black**). These traces diverge at approximately 18 h; however, similar trends are seen. The feedbacks associated with convection and precipitation formation affect the evolution of the cloud properties, leading to different LWP and IWPs. These differences are due to the influence of the domain size on, for example, cloud radiative cooling and entrainment, leading to the formation of different convective cells, of different sizes, to the original domain.

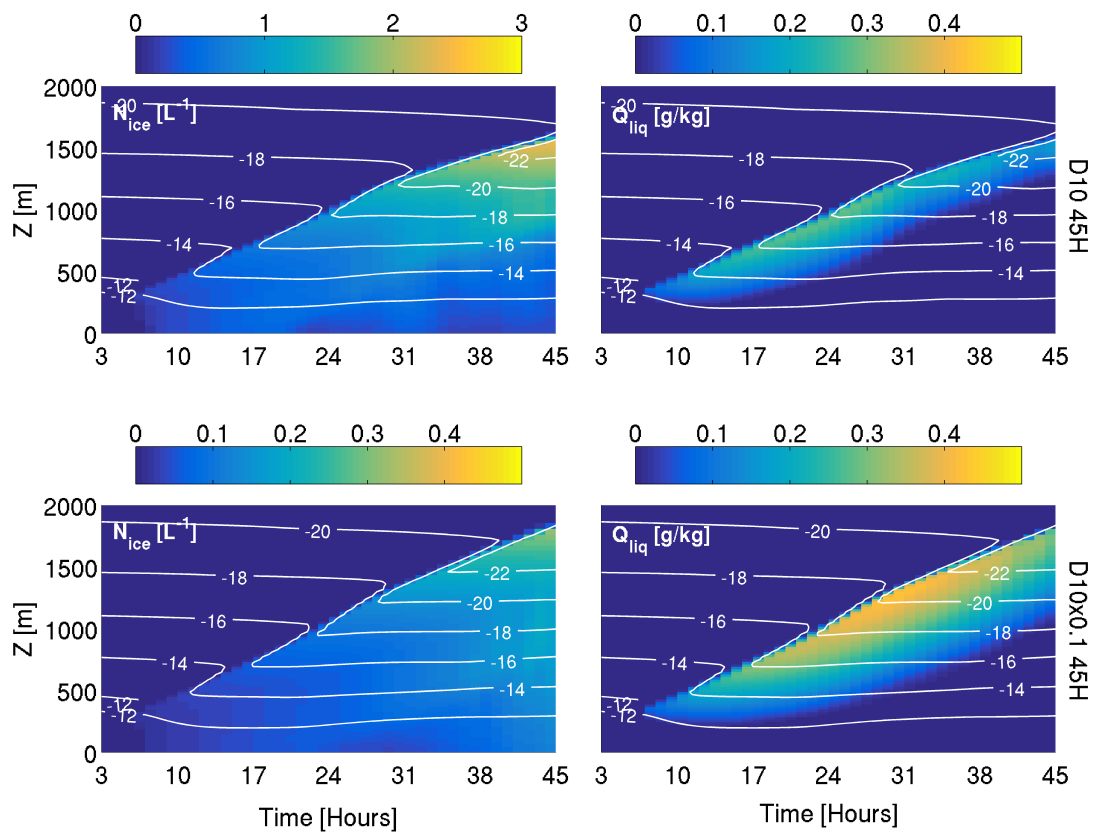


Figure S14. Modelled N_{ice} (left column) and Q_{liq} (right column) when using D10 (top row) and D10x0.1 (bottom row) to simulate case 2 over an extended run time of 45 h.

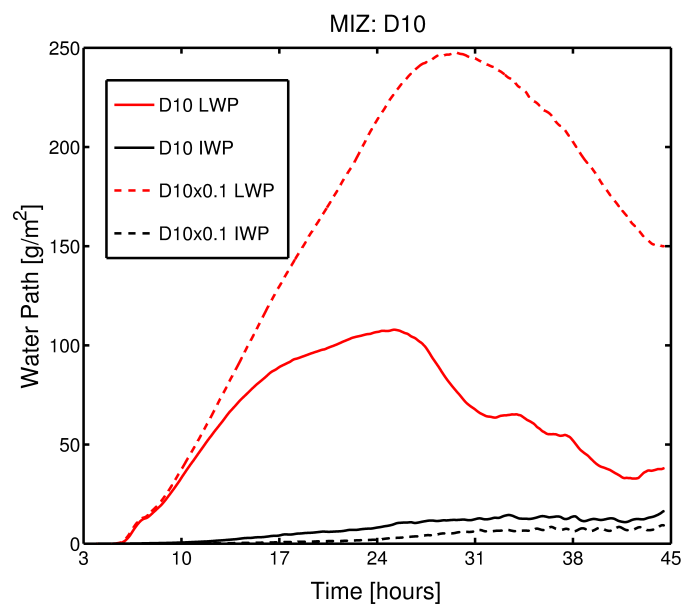


Figure S15. Modelled LWP (red) and IWP (black) when using D10 (**solid**) and D10×0.1 (**dashed**) to simulate case 2 over an extended run time of 45 h.

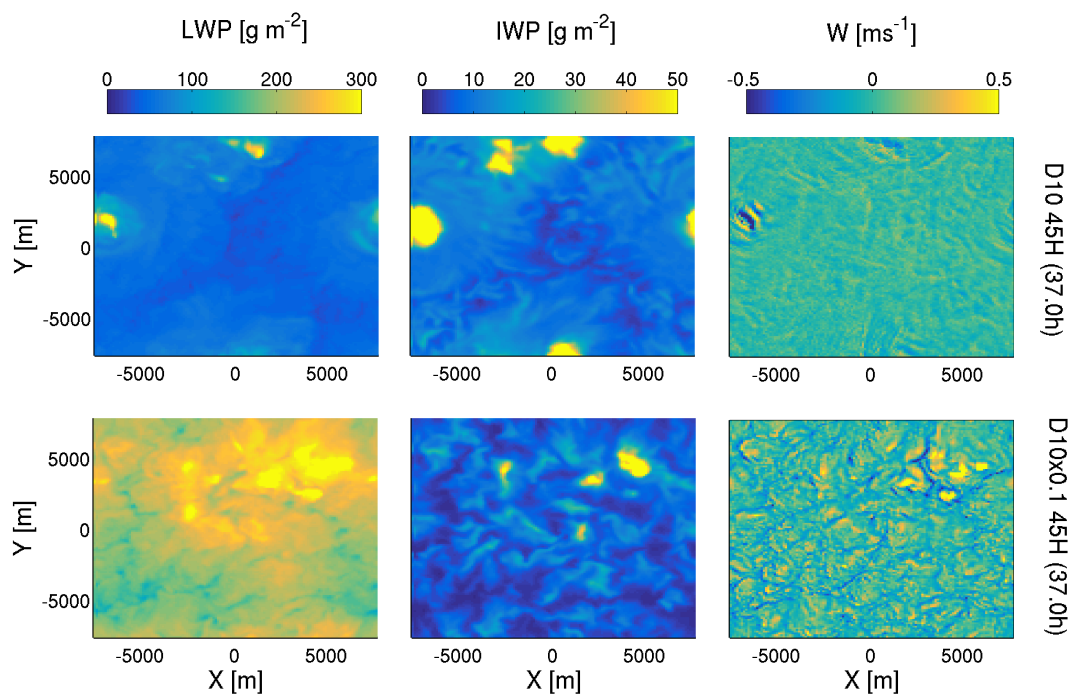


Figure S16. Modelled LWP (first column), IWP (second column), and vertical velocity (third column) at approximately 1500 m using D10 (top row) and D10×0.1 (bottom row) to simulate case 2. Planar X-Y slices are shown at 37 h.

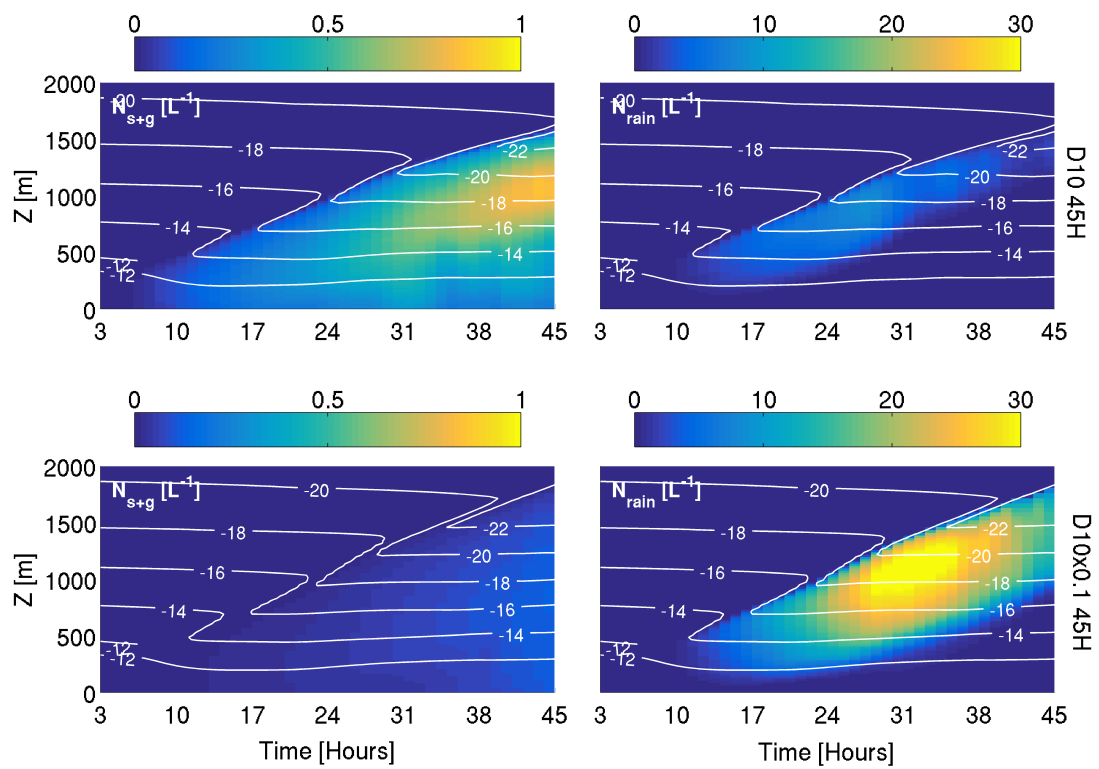


Figure S17. Modelled solid (N_{s+g} , **left column**) and liquid (N_{rain} , **right column**) precipitation when using D10 (**top row**) and D10 \times 0.1 (**bottom row**) to simulate case 2 over an extended run time of 45 h.